

Ali Osman Berk Şapcı

June 10, 2022

Contents

| | | |
|----------|---|-----------|
| 1 | Introduction | 1 |
| 1.1 | Challenges | 1 |
| 1.2 | Contributions | 1 |
| 2 | Biological Experiments and Data Collection | 2 |
| 3 | Feature Extraction | 3 |
| 3.1 | Preprocessing | 4 |
| 3.1.1 | Dealing with Occluded Body Parts | 4 |
| 3.1.2 | Aligning Different Orientations | 6 |
| 3.1.3 | Filtering and Imputation | 6 |
| 3.2 | Computation of Spatio-temporal Features | 7 |
| 3.2.1 | Distances Between Body Parts | 8 |
| 3.2.2 | Joint Angles Between Body Parts | 8 |
| 3.2.3 | Cartesian Pose Values of Body Parts | 8 |
| 3.2.4 | Constructing Spatio-temporal Feature Matrices | 9 |
| 3.3 | Computation of Dynamic Postural Features | 9 |
| 3.3.1 | Moving Statistics of Gradient Features | 9 |
| 3.3.2 | Wavelet Transformation of Snapshot Features | 10 |
| 3.3.3 | Constructing Dynamic Postural Feature Tensors | 12 |
| 3.4 | Computation of Behavioral Representations | 12 |
| 3.4.1 | Flattening Dynamic Postural Feature Tensors | 12 |
| 3.4.2 | L_1 Normalization of Frames | 12 |
| 4 | Experiment Outlining | 13 |
| 5 | Behavior Mapping | 14 |
| 5.1 | Computing Behavioral Embeddings | 14 |
| 5.1.1 | Supervised Disparate Embeddings | 14 |
| 5.1.2 | Supervised Joint Embeddings | 14 |
| 5.1.3 | Unsupervised Disparate Embeddings | 14 |
| 5.1.4 | Unsupervised Joint Embedding | 14 |
| 5.1.5 | Semi-supervised Pair Embeddings | 15 |
| 5.2 | Soft Clustering of Behavioral Embeddings | 15 |
| 5.2.1 | Disparate Clustering | 15 |
| 5.2.2 | Joint Clustering | 15 |
| 5.2.3 | Crosswise Clustering | 15 |
| 5.2.4 | Mapping Clusters to Behavioral Categories | 15 |

| | | |
|-----------|--|-----------|
| 5.2.5 | Computing Behavioral Scores | 16 |
| 5.3 | Nearest Neighbor Analysis and Classification | 16 |
| 5.3.1 | | 16 |
| 5.3.2 | | 17 |
| 6 | Analyzing Behavioral Repertoire of Asleep Fruit Fly | 18 |
| 7 | Employing Proposed Pipeline for Collected Data | 19 |
| 8 | Results | 20 |
| 9 | basty: A Software Package for Automated <u>B</u>ehavioral <u>A</u>nalysis of Asleep Fruit Fly | 21 |
| 10 | Conclusion | 22 |

List of Figures

| | | |
|-----|-----------------------|---|
| 1.1 | Orientations. | 1 |
|-----|-----------------------|---|

List of Tables

Abstract

A *Bastı* (English: *Basty*, Azerbaijani Turkish: *Basdı*, Anatolian Turkish: *Basdırık*) is an evil spirit in Turkic mythology which rides on people's chests while they sleep, bringing on nightmares. Bastı sits astride a sleeper's chest and becomes heavier until the crushing weight awakens the terrified and breathless dreamer. The victim awakes, unable to move under the Bastı's weight. It may also include lucid dreams.

Chapter 1

Introduction

1.1 Challenges

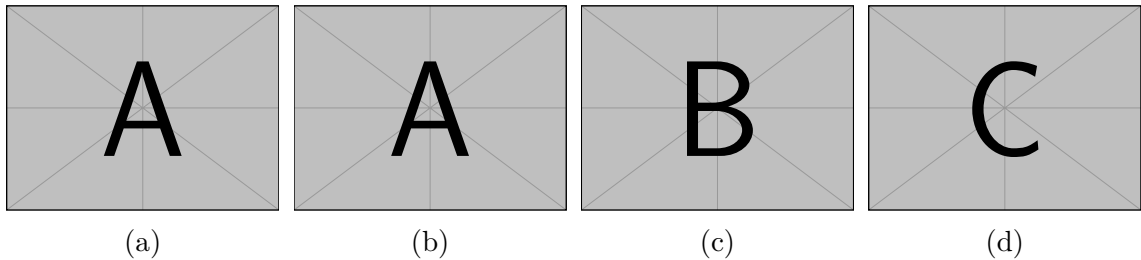


Figure 1.1: Orientations.

1.2 Contributions

Chapter 2

Biological Experiments and Data Collection

Chapter 3

Feature Extraction

For a single experiment data, i.e., single fruit fly recorded between ZT10 and ZT2 (zeitgeber time 10 and 2), feature extraction consists of four consecutive steps, where the input in one stage is the output of the previous one. The input of the first step is the raw output signal of the tracking and pose estimation model, in our case, the output of DeepLabCut, a toolbox for markerless pose estimation. The feature extraction steps are as follows:

1. Constructing pose values and preprocessing; dealing with occluded body parts, alignment of different orientations, filtering and imputation.
2. Computing spatio-temporal features, such as distances between body parts, velocity, angular velocity from body part positions.
3. Computing dynamic postural features by extending spatio-temporal features to multiple time-scales using wavelet transformation and sliding window statistics.
4. Computing normalized high-dimensional behavioral representations.

Matrices $\mathbf{X} \in \mathbb{R}^{T \times N}$ and $\mathbf{Y} \in \mathbb{R}^{T \times N}$ denotes a multivariate time series for x and y cartesian components of two-dimensional video recordings that are collected for N tracked body parts of the fly on T consecutive time stamps by a pose estimation model. This multivariate time series matrices \mathbf{X} and \mathbf{Y} are the raw input data that goes into the first step of the feature extraction. Note that the number of body parts, N , must be the same among all experiments conducted with different fruit flies, but the number of time stamps, T , might differ. Each column of the $\mathbf{X} = [\mathbf{x}_1, \dots, \mathbf{x}_N]^\top$ and $\mathbf{Y} = [\mathbf{y}_1, \dots, \mathbf{y}_N]^\top$ can be written respectively as follows:

$$\mathbf{y}_i = (y_{i,1}, y_{i,2}, \dots, y_{i,t-1}, y_{i,t}, y_{i,t+1}, \dots, y_{i,T}), \quad (3.1)$$

$$\mathbf{x}_i = (x_{i,1}, x_{i,2}, \dots, x_{i,t-1}, x_{i,t}, x_{i,t+1}, \dots, x_{i,T}). \quad (3.2)$$

Here i denotes the index of the body part, e.g., leg tip or proboscis.

In addition to \mathbf{X} and \mathbf{Y} , a pose estimation model may report prediction scores for each tracked body part at each time step, which is the case for DeepLabCut as well. $L \in \mathbb{R}^{N \times T}$ denotes the time series of prediction scores, each column of the $L = [\mathbf{l}_1, \dots, \mathbf{l}_N]^\top$ can be written as follows:

$$\mathbf{l}_i = (l_{i,1}, l_{i,2}, \dots, l_{i,t-1}, l_{i,t}, l_{i,t+1}, \dots, l_{i,T}). \quad (3.3)$$

The prediction scores tend to be very low when the body part is not visible. Thus, L provides valuable information about the occluded body parts. In the Section 3.1.1, how L is incorporated into construction of pose values is described in detail.

3.1 Preprocessing

The goal of in this step is to preprocess the signal, which involves filtering and imputation of certain video frames. But in addition to this, there are a couple of optional procedures that can be beneficial for our task of learning stereotypical behaviors. These additional procedures deal with occluded body parts of the fly, alignment of the fly orientations and defining new points of interest.

3.1.1 Dealing with Occluded Body Parts

As mentioned in the Section 1.1, the two-dimensionality of the video recordings introduces a number of important challenges, and one of them is the problem of occluded body parts. There are many types of occlusions, and some of them can be informally described as follows. One examples is short occlusions resulting from postural changes. Imputation of the time series \mathbf{X} and \mathbf{Y} for such short occlusions is relatively easy since the number of consecutive missing data points are not many. However, this is not the case for long occlusions, which usually occur when the fly is dormant for a long period of time. Especially for the body parts which have left and right counterparts, it is usual that the orientation of the fly results in one of the counterparts being occluded in long dormant epochs. We follow multiple approaches to handle different type occlusions; namely imputation and elimination of corresponding data-points. Before describing those approaches, we define a criterion for being occluded.

Oriented Pose Values for Body Parts with Left & Right Counterparts

If the fly is oriented perpendicular to the camera perspective, as in Figure 1.1d, then one of the left and right body parts is often occluded. In other orientations (e.g., Figure 1.1a and Figure 1.1c), both of them or none of them might be occluded as well. However, in the conducted experiments, flies usually choose to stay dormant perpendicular to the camera perspective in long dormant epochs, as mentioned in Chapter 2. In such cases, one can concede to use only one of the left and right counterparts to construct pose values. Therefore, this optional step is included in the behavioral mapping pipeline to reduce pose values of body parts with left and right counterparts to a single value.

We use prediction scores to determine which body part should be used to compute oriented pose values. Let i and j be a pair of body parts which are left and right counterparts of each other, e.g., left haltere and right haltere. Then, one can use the \mathbf{l}_i and \mathbf{l}_j to predict if one of them is occluded at a particular time step t . Let $\text{orient}(\mathbf{x}_i, \mathbf{x}_j)$ ($\text{orient}(\mathbf{y}_i, \mathbf{y}_j)$) be a new pose vector which will be computed based on \mathbf{x}_i and \mathbf{x}_j (\mathbf{y}_i and \mathbf{y}_j), e.g., a vector of oriented haltere pose values, composed of

left haltere and right haltere pose values. The following conditional procedures are proposed to compute oriented pose values from left and right pose values by deciding the orientation of the fly for a counterpart body pair. The procedures below can be used separately, or successively.

- If $l_{i,t} - l_{j,t} \geq \epsilon$, then, without loss of generality, $\text{orient}(\mathbf{x}_i, \mathbf{x}_j)_t = x_{i,t}$ and $\text{orient}(\mathbf{y}_i, \mathbf{y}_j)_t = y_{i,t}$ for a threshold ϵ , typically $\epsilon > 0.5$.
- If $|\{t' : l_{i,t'} > l_{j,t'}, t' \in [t - \tau .. t + \tau]\}| > \tau$, then, without loss of generality, $\text{orient}(\mathbf{x}_i, \mathbf{x}_j)_t = x_{i,t}$ and $\text{orient}(\mathbf{y}_i, \mathbf{y}_j)_t = y_{i,t}$, for a window of size $2w + 1$.
- If $l_{i,t} > l_{j,t}$ and if the nearest confident left orientation is closer than the nearest confident right orientation, i.e.,

$$\arg \min_{t'} \{ |t - t'| : l_{i,t'} - l_{j,t'} \geq \epsilon \} > \arg \min_{t'} \{ |t - t'| : l_{j,t'} - l_{i,t'} \geq \epsilon \},$$

then, without loss of generality, $\text{orient}(\mathbf{x}_i, \mathbf{x}_j)_t = x_{i,t}$ and $\text{orient}(\mathbf{y}_i, \mathbf{y}_j)_t = y_{i,t}$.

- If simply $l_{i,t} > l_{j,t}$, then without loss of generality, $\text{orient}(\mathbf{x}_i, \mathbf{x}_j)_t = x_{i,t}$ and $\text{orient}(\mathbf{y}_i, \mathbf{y}_j)_t = y_{i,t}$.

Except directly comparing the prediction confidence scores as in the last procedure, some of the time points might be left with undecided orientations. If the number of such time points is acceptable, then directly comparing the prediction scores for those time points is convenient and handy.

After applying the above procedures for a left and right counterpart pair i and j , we can define oriented multivariate time series as

$$\begin{aligned} \mathbf{X}^o &= \left(\left[(\mathbf{x}_k)_{k \notin \bigcup_{\{i,j\} \in \mathcal{O}} \{i,j\}} \right]^\top \middle| \left[(\text{orient}(\mathbf{x}_i, \mathbf{x}_j))_{\{i,j\} \in \mathcal{O}} \right]^\top \right), \\ \mathbf{Y}^o &= \left(\left[(\mathbf{y}_k)_{k \notin \bigcup_{\{i,j\} \in \mathcal{O}} \{i,j\}} \right]^\top \middle| \left[(\text{orient}(\mathbf{y}_i, \mathbf{y}_j))_{\{i,j\} \in \mathcal{O}} \right]^\top \right), \end{aligned}$$

where \mathcal{O} is the set of index pairs of left and right counterparts and $\bigcup_{\{i,j\} \in \mathcal{O}} \{i,j\}$ is the union of all indexes of such body parts pairs. Applying described procedures for each left and right counterparts results in computing \mathbf{X}^o and \mathbf{Y}^o . This oriented versions of original data matrices can be used instead of \mathbf{X} and \mathbf{Y} in the rest of the pipeline, if desired.

Detecting Occlusions Using Prediction Scores & Anomalous Pose Values

Major postural changes and overlapping body parts during movements result in some body parts being occluded for a short interval of time. These types of occlusions may span several frames to several seconds. Since the pose estimation model makes predictions for such data points, it is necessary to detect and process such data points. Our pipeline exploits two indicators for detection: prediction scores and anomalous changes in pose values. We mark the body parts estimated to be occluded and corresponding time intervals, and then the desired imputation method is used to fill those time intervals appropriately.

The following conditions are considered to detect occluded body parts, note that they can be used separately or in combination with each other.

- If the prediction confidence score at time step t is lower than a given threshold ϵ , then the t is marked to be imputed.
- If z -score of the prediction confidence score $l_{i,t}$ computed within a window with size τ , and centered at t , is lower than a given threshold ϵ_z , then the t is marked to be imputed.
- If the second-order gradient of the estimated pose value exceeds a given threshold δ , then the t is marked to be imputed.
- If the difference between estimated pose value at time step t and median of pose values within the window of size τ , centered at time step t , exceeds the threshold δ , then the t is marked to be imputed.

Here, the window sizes and threshold parameters are determined separately for each condition. The conditions described above are useful not only for occluded body parts, but are also beneficial for tackling unnatural and abnormal predictions made by the pose estimation model.

3.1.2 Aligning Different Orientations

It may be desired to align different orientations and postures in some cases. For instance, it is not possible to interpret vertical and horizontal replacements of body parts separately without aligning them into a reference frame. Because flies can position themselves in different orientations while exhibiting similar actions, as it can be seen from the Figure 1.1a and Figure 1.1b.

To rotationally align each frame, we transformed body part coordinate values into an egocentric reference frame centered on the middle of the fly’s spine, e.g., a line along the thorax. Then, we performed a linear transformation to all pose values in order to place the spine at the origin, oriented along the y -axis.

Alignment of the frames is an optional step in the behavioral mapping pipeline. It is potentially beneficial and reasonable to perform alignment when the cartesian pose values of the body parts are included as spatio-temporal features.

3.1.3 Filtering and Imputation

Estimated pose values are highly noisy because of the reasons explained in Section 1.1. Thus, filtering the pose values and imputation of the data points marked as occluded or abnormal is an essential step before proceeding with the rest of the pipeline, which contains stages that are sensitive to noise.

One of the most practical and effective approaches for time series imputation is applying interpolation. We also benefit from univariate interpolation to replace values at marked time points, where the exact algorithm is chosen to be one of the followings; linear interpolation, spline interpolation, forward filling, and backward filling.

After imputation, we apply a median filter with appropriate window size and smooth each \mathbf{x}_i and \mathbf{y}_i separately. Finally, a boxcar filter (moving average) with a relatively small window size is used to filter out rapidly changing signals by averaging. We

observed that large window sizes may result in smoothing out some critical signals, which potentially define short-duration low-amplitude behaviors, e.g., switch-like haltere movement behavior.

A Rauch-Tung-Striebel Kalman smoother [Rauch et al., 1965] is employed in the development stage. However, no significant performance improvement is observed, and hence, later abandoned due to its computational cost and requirement of setting the various state parameters to reasonable values.

The configuration and actual parameters of the imputation methods and the filters are given in Chapter 7, together with some representative examples demonstrating the effect of preprocessing with different configurations.

3.2 Computation of Spatio-temporal Features

After preprocessing of pose values, it is now feasible to go one step further towards learning stereotypical behaviors. Although tracking of relevant body parts and processing corresponding pose values is an essential step for quantifying behavior, a set of coordinate values is not sufficient to represent and capture complex spatio-temporal dynamics of animal behavior. There are thousands of unique postures, and behaviors are not even exhibited by some static set of postures. Instead, they are defined by expressive and meaningful spatio-temporal features such as distances, velocities, angles, and angular velocities. Therefore, one needs to compute such features from the coordinate values of body parts in two-dimensional space.

The second stage of the feature extraction is computation of spatio-temporal features from pose values. Two type of features are computed in this stage, as listed below.

1. **Snapshot features:** Spatio-temporal feature values computed at a snapshot of time, listed as follows:
 - distances,
 - angles,
 - cartesian pose values (i.e., per body part features).
2. **Gradient features:** Spatio-temporal feature values computed based how snapshot features change over time, listed as follows:
 - change of distances,
 - change of angles (i.e., angular velocities),
 - change of cartesian pose values (i.e., body part velocities).

The gradients of snapshot features are computed using second-order accurate central differences in the interior points. The resulting gradient features have the same shape, i.e., the number of features and the number of time-stamps, as the snapshot features.

3.2.1 Distances Between Body Parts

Given a body part pair (i, j) , the distance between them at a time step t is calculated as a usual Euclidean distance, given below,

$$d_t^{i,j} = \sqrt{(x_{i,t} - x_{j,t})^2 + (y_{i,t} - y_{j,t})^2}. \quad (3.4)$$

The corresponding gradient feature, namely the change of distance between body part i and j , is computed using the second-order gradient approximation,

$$d_t^{i,j} = \begin{cases} \frac{|d_{t+1}^{i,j} - d_t^{i,j}|}{\Delta t} & \text{if } t=0 \text{ or } t=T, \\ \frac{|d_{t+1}^{i,j} - d_{t-1}^{i,j}|}{2\Delta t} & \text{otherwise,} \end{cases} \quad (3.5)$$

where Δt is the sampling period, and it is equal to $1/\text{FPS}$ seconds.

3.2.2 Joint Angles Between Body Parts

Given a triplet of body parts (i, j, k) , angle between i and k around j is computed using the 2-argument arctangent function as given below,

$$\omega_t^{i,j,k} = \text{atan2} \left(\det \begin{bmatrix} x_{i,t} - x_{j,t} & x_{k,t} - x_{j,t} \\ y_{i,t} - y_{j,t} & y_{k,t} - y_{j,t} \end{bmatrix}, \begin{bmatrix} x_{i,t} - x_{j,t} \\ y_{i,t} - y_{j,t} \end{bmatrix} \cdot \begin{bmatrix} x_{k,t} - x_{j,t} \\ y_{k,t} - y_{j,t} \end{bmatrix} \right) + \pi. \quad (3.6)$$

Then, similar to the change of distance features, angular velocities are approximated by

$$\dot{\omega}_t^{i,j,k} = \begin{cases} \frac{|\omega_{t+1}^{i,j,k} - \omega_t^{i,j,k}|}{\Delta t} & \text{if } t=0 \text{ or } t=T, \\ \frac{|\omega_{t+1}^{i,j,k} - \omega_{t-1}^{i,j,k}|}{2\Delta t} & \text{otherwise.} \end{cases} \quad (3.7)$$

3.2.3 Cartesian Pose Values of Body Parts

Cartesian pose values of a body part i is straightforwardly given by the x and y coordinate values as follows:

$$x_t^i = x_{i,t}, \quad (3.8)$$

$$y_t^i = y_{i,t}. \quad (3.9)$$

Note that for a single body part, two feature values are generated. Corresponding gradient features, namely the body part velocities along each cartesian component, are computed by

$$\dot{x}_t^i = \begin{cases} \frac{x_{t+1}^i - x_t^i}{\Delta t} & \text{if } t=0 \text{ or } t=T, \\ \frac{x_{t+1}^i - x_{t-1}^i}{2\Delta t} & \text{otherwise,} \end{cases} \quad (3.10)$$

$$\dot{y}_t^i = \begin{cases} \frac{y_{t+1}^i - y_t^i}{\Delta t} & \text{if } t=0 \text{ or } t=T, \\ \frac{y_{t+1}^i - y_{t-1}^i}{2\Delta t} & \text{otherwise.} \end{cases} \quad (3.11)$$

In order to compute overall two-dimensional velocity of a body part, one can always use the distance between origin and corresponding body part.

3.2.4 Constructing Spatio-temporal Feature Matrices

Let \mathcal{C}, \mathcal{D} , and \mathcal{A} denote the sets of body parts, body part pairs, and body part triplets; respectively defining cartesian pose values, distances, and angles. Similarly, let $\mathcal{C}', \mathcal{D}'$, and \mathcal{A}' denote sets which define sets of respective gradient features. Then snapshot feature matrix \mathbf{S} constructed as follows;

$$\mathbf{S} = \left([(\mathbf{x}^i)_{i \in \mathcal{C}}] \mid [(\mathbf{y}^i)_{i \in \mathcal{C}}] \mid [(\mathbf{d}^{i,j})_{\{i,j\} \in \mathcal{D}}] \mid [(\boldsymbol{\omega}^{i,j,k})_{\{i,j,k\} \in \mathcal{A}}] \right), \quad (3.12)$$

where the vectors are defined as $\mathbf{x}^i = [x_1^i, \dots, x_T^i]$, $\mathbf{y}^i = [y_1^i, \dots, y_T^i]$, $\mathbf{d}^{i,j} = [d^{i,j}, \dots, d_T^{i,j}]$, and $\boldsymbol{\omega}^{i,j,k} = [\omega_1^{i,j,k}, \dots, \omega_T^{i,j,k}]$.

Similarly, for gradient features, the feature matrix is constructed by concatenating change of distances, angular velocities and body part velocities; given by

$$\mathbf{G} = \left([(\dot{\mathbf{x}}^i)_{i \in \mathcal{C}'}] \mid [(\dot{\mathbf{y}}^i)_{i \in \mathcal{C}'}] \mid [(\dot{\mathbf{d}}^{i,j})_{\{i,j\} \in \mathcal{D}'}] \mid [(\dot{\boldsymbol{\omega}}^{i,j,k})_{\{i,j,k\} \in \mathcal{A}'}] \right), \quad (3.13)$$

where the vectors are defined as $\dot{\mathbf{x}}^i = [\dot{x}_1^i, \dots, \dot{x}_T^i]$, $\dot{\mathbf{y}}^i = [\dot{y}_1^i, \dots, \dot{y}_T^i]$, $\dot{\mathbf{d}}^{i,j} = [\dot{d}^{i,j}, \dots, \dot{d}_T^{i,j}]$, and $\dot{\boldsymbol{\omega}}^{i,j,k} = [\dot{\omega}_1^{i,j,k}, \dots, \dot{\omega}_T^{i,j,k}]$.

The resulting two feature matrices are $\mathbf{S} \in \mathbb{R}^{T \times (2|\mathcal{C}| + |\mathcal{D}| + |\mathcal{A}|)}$, namely snapshot feature matrix, and $\mathbf{G} \in \mathbb{R}^{T \times (2|\mathcal{C}'| + |\mathcal{D}'| + |\mathcal{A}'|)}$, namely gradient feature matrix. Let N_S denote the number of snapshot features, being equal to $2|\mathcal{C}| + |\mathcal{D}| + |\mathcal{A}|$ and let N_G denote the number of gradient features, which is equal to $2|\mathcal{C}'| + |\mathcal{D}'| + |\mathcal{A}'|$.

3.3 Computation of Dynamic Postural Features

Instantaneous values of spatio-temporal features do not provide a sufficient description of complex postural dynamics of behaviors. Understanding the output of a complex biological system, in our case behavior, can only be achieved by studying multiple time-scales together. Previous studies attempt to search behavioral motifs, e.g., repeated sub-sequences of actions with finite length, within the behavioral time series [CITE]. However, as Berman et al. [2014] states, this paradigm usually requires problems of temporal alignment and relative phasing between different scales. Alternatively, extending spatio-temporal features to capture postural dynamics at different time-scales eliminate requirements of temporal alignment and motif based analysis. In order to extend the spatio-temporal features to dynamic postural features, we applied wavelet transformation (similar to Berman et al. [2014]) and computed moving statistics at different time-scales (similar to Kabra et al. [2013]), respectively for snapshot feature set (\mathbf{S}) and gradient feature set (\mathbf{G}).

3.3.1 Moving Statistics of Gradient Features

Gradient features only reflect the instantaneous values of velocities with respect to the sampling rate. In order to capture how these values change within a given interval, the moving statistics, e.g., mean and standard deviation, of gradient features are computed with a sliding window approach. Let τ be the window size parameter, i.e., the timescale of interest, then the moving mean of the corresponding gradient

feature \mathbf{g}_i is given by the function μ_τ :

$$\mu_\tau(g_{i,t}) = 1/\min\{t+\tau, T\} - \max\{t-\tau, 1\} + 1 \sum_{t'=\max\{t-\tau, 1\}}^{\min\{t+\tau, T\}} g_{i,t'}. \quad (3.14)$$

Similarly, the moving standard deviation of a gradient feature $g_{i,t}$ by is computed by σ_τ , as in the below equation.

$$\sigma_\tau(g_{i,t}) = \left(1/\min\{t+\tau, T\} - \max\{t-\tau, 1\} + 1 \sum_{t'=\max\{t-\tau, 1\}}^{\min\{t+\tau, T\}} (\mu_\tau(g_{i,t}) - g_{i,t'})^2 \right)^{1/2} \quad (3.15)$$

Moving statistics feature generation approach is used to learn animal behavior by Kabra et al. [2013], and Marshall et al. [2021] is also included such features into the analysis.

3.3.2 Wavelet Transformation of Snapshot Features

The wavelet domain is a useful representation of postural dynamics due to the following reasons given by Berman et al. [2014], and proposed spectrogram generation is used by others as well [Marshall et al., 2021, Todd et al., 2017].

- It describes dynamics over multiple time-scales simultaneously by possessing a multi-resolution time-frequency trade-off.
- It eliminates the requirement of precise temporal alignment for capturing periodic behaviors by taking amplitudes of the continuous wavelet transform of each snapshot feature at different scales.

Given a function $s(t)$, continuous wavelet transformation at a frequency $f > 0$ is expressed by the following integral:

$$W_{f,t'}[s(t)] = \frac{1}{\sqrt{a(f)}} \int_{-\infty}^{\infty} s(t) * \left(\frac{t-t'}{a(f)} \right) dt, \quad (3.16)$$

where Ψ is the wavelet function and a is a function for converting frequencies to wavelet scale factor. The Morlet wavelet is suitable for describing postural dynamics which is closely related to human perception, both hearing and vision [Daugman, 1985], and is used in the pipeline. The corresponding wavelet function is given by

$$\Psi(t) = \exp\left\{\frac{t^2}{2}\right\} \cos(w_0 t), \quad (3.17)$$

where w_0 is a non-dimensional parameter. The frequency to scale conversion function a for Morlet wavelet is as follows:

$$a(f) = \frac{w_0 + \sqrt{2 + w_0^2}}{4\pi f}. \quad (3.18)$$

For the discrete sequence of snapshot feature \mathbf{s}_i with sampling period Δt , $W_{f,t'}[s(t)]$ translates into

$$W_f(\mathbf{s}_i, t') = \frac{1}{\sqrt{a(f)}} \sum_{t=1}^T \Delta t s_{i,t} * \left(\frac{t-t'}{af} \right), \quad (3.19)$$

where $t', t \in \mathbb{Z}$ and $1 \leq t' \leq T$ [Torrence and Compo, 1998].

Normalization of Wavelet Power Spectrum

In order to ensure that wavelet transforms (Equation 3.19) at each frequency f are directly comparable to each other and to the other transformed time series, the transformation W_f has to be normalized at each frequency f to have unit energy. This normalization for Morlet wavelet at frequency f is as follows:

$$C(f) = \frac{\pi^{-\frac{1}{4}}}{\sqrt{2a(f)}} \exp \left\{ \frac{1}{4} \left(w_0 - \sqrt{w_0^2 + 2} \right)^2 \right\}. \quad (3.20)$$

So resulting normalized transformation, which is also used to generate the spectrogram in Berman et al. [2014], is given by

$$W_f^0(\mathbf{s}_i, t') = \frac{1}{C(f)} |W_f(\mathbf{s}_i, t')|. \quad (3.21)$$

In addition to the above conventionally used normalization, we alternatively adopted the normalization proposed by Liu et al. [2007]. According to this alternative adjustment, the wavelet power spectrum should be equal to the transform coefficient squared divided by the scale it associates.

$$W_f^0(\mathbf{s}_i, t') = \frac{W_f(\mathbf{s}_i, t')^2}{a(f)} \quad (3.22)$$

We observed substantial improvements using this power spectrum (see Section 7).

Determining Spectrum Frequencies

We investigate two different approaches for computing a set of frequencies and, we include both of them in the behavior mapping pipeline. One set is dyadically spaced frequencies between f_{\min} and f_{\max} via

$$f_i = f_{\max} 2^{-\frac{i-1}{N_f-1} \log \frac{f_{\max}}{f_{\min}}}, \quad (3.23)$$

where $f_{\max} = FPS/2$ Hz is the Nyquist frequency.

The other alternative set of frequencies is linearly spaced between f_{\min} and f_{\max} by

$$f_i = f_{\min} + \frac{f_{\max} - f_{\min}}{N_f - 1} i, \quad (3.24)$$

for $i = 1, 2, \dots, N_f$, and their corresponding wavelet scales are computed via $a(f_i)$.

3.3.3 Constructing Dynamic Postural Feature Tensors

Let $\mathcal{T}_S = \{1/f_{\min}, \dots, 1/f_{\max}\}$ and $\mathcal{T}_G = \{\tau_{\min}, \dots, \tau_{\max}\}$ denote the time-scale sets respectively for wavelet transforms of snapshot features and moving statistics of gradient features. Then corresponding feature tensors are given as follows:

$$\mathbf{W} = \left(W_f^0(\mathbf{s}_i, t) \right)_{1 \leq t \leq T, 1/f \in \mathcal{T}_S, 1 \leq i \leq N_S}, \quad (3.25)$$

$$\mathbf{M}_\mu = \left(\mu_\tau(g_{i,t}) \right)_{1 \leq t \leq T, \tau \in \mathcal{T}_G, 1 \leq i \leq N_G}, \quad (3.26)$$

$$\mathbf{M}_\sigma = \left(\sigma_\tau(g_{i,t}) \right)_{1 \leq t \leq T, \tau \in \mathcal{T}_G, 1 \leq i \leq N_G}. \quad (3.27)$$

The resulting extended feature tensors of dynamic postural representations are $\mathbf{W} \in \mathbb{R}^{T \times |\mathcal{T}_S| \times N_S}$, $\mathbf{M}_\mu \in \mathbb{R}^{T \times |\mathcal{T}_G| \times N_G}$ and $\mathbf{M}_\sigma \in \mathbb{R}^{T \times |\mathcal{T}_G| \times N_G}$.

3.4 Computation of Behavioral Representations

After applying wavelet transformation or computing moving statistics to extend extracted spatio-temporal features to dynamic postural features, a couple of additional operations are required to continue in the behavior mapping pipeline.

3.4.1 Flattening Dynamic Postural Feature Tensors

As constructed in Section 3.3, dynamic postural feature tensors are $\mathbf{W} \in \mathbb{R}^{T \times |\mathcal{T}_S| \times N_S}$, $\mathbf{M}_\mu \in \mathbb{R}^{T \times |\mathcal{T}_G| \times N_G}$, and $\mathbf{M}_\sigma \in \mathbb{R}^{T \times |\mathcal{T}_G| \times N_G}$. In order to apply manifold learning-based dimensionality reduction algorithms or traditional machine learning algorithms such as decision trees, the last two dimensions of these feature tensors needs to be flattened. As a result, feature matrices are $\mathbf{W}^* \in \mathbb{R}^{T \times (N_S |\mathcal{T}_S|)}$, $\mathbf{M}_\mu^* \in \mathbb{R}^{T \times (N_G |\mathcal{T}_G|)}$ and $\mathbf{M}_\sigma^* \in \mathbb{R}^{T \times (N_G |\mathcal{T}_G|)}$ are obtained.

3.4.2 L_1 Normalization of Frames

Dynamic postural feature distributions of similar behaviors may differ among flies due to different characteristics such as gender, and being sleep-deprived. Due to the two-dimensional nature of the video recordings, different orientations may cause observing different feature values for the same behavior. In order to have a homogeneous feature space among flies and along the time, at each time step t , L_1 normalization is applied as follows:

$$\hat{\mathbf{w}}_i = \left(\frac{w_{t,i}^*}{\sum_{j=1}^{N_S |\mathcal{T}_S|} w_{t,j}^*} \right)_{1 \leq t \leq T} \quad \text{and} \quad \hat{\mathbf{W}} = \left[(\hat{\mathbf{w}}_i)_{1 \leq i \leq N_S |\mathcal{T}_S|} \right]. \quad (3.28)$$

Similarly, L_1 normalized versions of \mathbf{M}_μ^* and \mathbf{M}_σ^* , namely $\hat{\mathbf{M}}_\mu$ and $\hat{\mathbf{M}}_\sigma$ are obtained. Here $\hat{\mathbf{W}}$, $\hat{\mathbf{M}}_\mu$ and $\hat{\mathbf{M}}_\sigma$ are the final multivariate time series of normalized high dimensional behavioral representation of a single experiment data, i.e., single fruit fly recorded between ZT10 and ZT2. Notice that, we may treat each time step, i.e., frame, as a discrete probability distribution after L_1 normalization.

Chapter 4

Experiment Outlining

Chapter 5

Behavior Mapping

5.1 Computing Behavioral Embeddings

McInnes et al. [2020] McInnes et al. [2017] Campello et al. [2013]

5.1.1 Supervised Disparate Embeddings

[NOTE: We compute Supervised-UMAP embeddings separately for each experiment. Computing supervised embeddings is only possible for annotated experiments. This is useful for exploring behavioral sub-categories. For instance, one annotation category, e.g. "grooming", can be consisted of two different clusters in the behavioral embedding space. We can further investigate how high-level behavioral annotations contain different but similar behaviors.]

5.1.2 Supervised Joint Embeddings

[NOTE: We compute Supervised-UMAP embeddings of all annotated experiments together. There is no specific benefit or use case (except visualization purposes) for computing this. The resulting embedding usually is not homogeneous in terms of fly experiments. Different flies do not mix well in the behavioral space.]

5.1.3 Unsupervised Disparate Embeddings

[NOTE: For each experiment, we compute a usual unsupervised embedding separately.]

5.1.4 Unsupervised Joint Embedding

[NOTE: We compute a single behavioral embedding using all experiments. The problem with this approach is that embedding space is too crowded and thus we can not find meaningful and homogeneous clusters right away. This embedding might be useful for visualization purposes.]

5.1.5 Semi-supervised Pair Embeddings

[NOTE: This is the novel and most useful embedding approach that we finally utilize to label unannotated experiments using annotated ones. We compute an embedding for each annotated and unannotated pair. For example, if there are N_A annotated experiments and N_U unannotated experiments we compute $N_A \cdot N_U$ embeddings in total. There are number of advantageous of this approach. Especially when, an behavioral repertoire of an annotated an unannotated are similar, resulting embedding is easy to interpret and use for clustering etc.]

5.2 Soft Clustering of Behavioral Embeddings

[NOTE: We always use soft clustering feature of HDBSCAN, since it is very beneficial to have a composite assignment for a data-point. For example, 0.7 grooming, 0.3 proboscis pumping may indicate that those two behaviors are simultaneously exhibited or a combination of both is exhibited etc. We can always take arg max if a categorical label is needed.]

5.2.1 Disparate Clustering

[NOTE: If embedding is a disparate embedding, then we directly cluster each of them separately. If a joint embedding or pair embedding will be clustered, then experiments need to be extracted from the embedding space first and then they need to be clustered separately.]

5.2.2 Joint Clustering

[NOTE: This is only applicable to joint and pair embeddings. We cluster all experiments in the behavioral embedding together.]

5.2.3 Crosswise Clustering

[NOTE: This is again only applicable to joint and pair embeddings. For joint embeddings, we exclude a sub-group of experiments. For pair embeddings, we exclude one of the pair experiments. Then rest of the embedding is clustered and clusters are formed. Finally for each excluded embedding, soft cluster memberships vectors are computed based on the formed clusters.]

5.2.4 Mapping Clusters to Behavioral Categories

[NOTE: If a clustering contains annotated experiments, we map that clusters in that clustering to a behavioral composition as follows (*subject to change, there are couple of alternatives*)

$$m_\alpha = \frac{\text{number of frames with annotation } \alpha \text{ in the cluster}}{\text{total number of frames with annotation } \alpha}. \quad (5.1)$$

So for each cluster, we end up with a vector $\mathbf{m} = (m_\alpha)$, represent it behavioral composition.]

5.2.5 Computing Behavioral Scores

[NOTE: Behavioral score of unannotated experiment will be computed using clustering membership score and behavioral composition mapping of those clusters. For example, using semi-supervised pair embeddings and crosswise clustering; one can compute behavioral scores for a frame as follows;

$$y_\alpha = \sum_{c=0}^C m_\alpha^c \quad (5.2)$$

where C is the number of clusters, \mathbf{m}^c is the behavioral composition of cluster c . As a result, for each frame we end up with a behavioral score vector $\mathbf{y} = (y_\alpha)$.]

5.3 Nearest Neighbor Analysis and Classification

5.3.1

Consider two experiments, an annotated one expt^+ , and an unannotated one expt^- , and their semi-supervised pair embeddings, respectively $\mathbf{E}^+ = [\mathbf{e}_1^+, \dots, \mathbf{e}_{F^+}^+]$ and $\mathbf{E}^- = [\mathbf{e}_1^-, \dots, \mathbf{e}_{F^-}^-]$, where F^+ and F^- are the total numbers of data points, e.g., frames, estimated as dormant and active. Given the true annotations \mathbf{y}^+ of expt^+ , and K behavioral categories, the goal is to compute $\hat{\mathbf{b}}_f = [\hat{b}_{f,1}, \dots, \hat{b}_{f,K}]$, representing the weights (in other words similarity score) of each behavioral categories, for expt^- , using \mathbf{E}^+ , \mathbf{E}^- and \mathbf{y}^+ .

The procedure start by constructing k -nearest neighbor graph using \mathbf{E}^+ and \mathbf{E}^- , and $k\text{-NN}(f)$ denotes the set of indices of \mathbf{e}_f^- 's k nearest neighbors. Then, initial $k\text{-NN}$ weight $b_{f,i}$ for each query point (i.e., frame) f of expt^- , and behavioral category i , is computed by

$$b_{f,i} = \begin{cases} \sum_{f' \in k\text{-NN}_i(f)} \frac{1}{d(\mathbf{e}_f^-, \mathbf{e}_{f'}^+)^p + \epsilon} & \text{if } |k\text{-NN}_i(f)| \neq 0, \\ 0 & \text{if otherwise,} \end{cases} \quad \text{where } p \in \{0, 1, 2\}. \quad (5.3)$$

Here, $k\text{-NN}_i(f) = \{f' : y_{f'}^+ = i, \text{ and } f' \in k\text{-NN}(f)\}$, is the set of indices of data points of expt^+ whose annotation is behavior category i , and is one of the k nearest neighbors of \mathbf{e}_f^- . $d(\mathbf{e}_f^-, \mathbf{e}_{f'}^+)$ is the euclidean distance between \mathbf{e}_f^- and $\mathbf{e}_{f'}^+$, and p parameterises the relation between distance and weight $b_{f,i}$. We add a small number ϵ (10^{-6}) to the denominator to avoid numerical errors. Resulting vector $\mathbf{b}_f = [b_{f,1}, \dots, b_{f,K}]$ weights the similarity of frame f to each behavioral category in the shared embeddings space based on the nearest neighbors.

Naturally, the number of occurrences of durations of the behavior bouts are different for each behavioral category, and therefore, \mathbf{y}^+ is highly imbalanced. As a results, number of nearest neighbors and \mathbf{b}_f are biased in favour of frequently occurring and long-bout behaviors. For instance, pumping-like movement of proboscis occur more frequently in longer bouts than switch-like movement of haltere. Especially when the k is large, it becomes crucial to consider the imbalanced distribution of behavior occurrences, since the embedding space will be dominated by frequent behaviors.

Thus, incorporating this imbalance to the formulation may help to improve the recall of rarely occurring short-bout behaviors and precision of frequently occurring long-bout behaviors. To achieve this, we normalize previously computed scores $b_{f,i}$ by a function of number of occurrences of behavioral category i as follows:

$$b'_{f,i} = \frac{b_{f,i}}{(1 + N_i^+)^p} \quad \text{or} \quad \frac{b_{f,i}}{\log_k(1 + N_i^+)} \quad \text{where} \quad p \in \{0, 1/2, 1\}, k \in \{2, 10\}, \quad (5.4)$$

where $N_i^+ = |\{f : y_f^+ = i\}|$ is the number of frames annotated as behavioral category i . In the above equation, two different alternatives are given for this normalization step; a polynomial one and a logarithmic one, where p and k parameterise the relation between N_i^+ and $b'_{f,i}$. For instance, if one is mostly interested in achieving high recall for frequently occurring behaviors, low p values or using the logarithmic alternative might be more appropriate. It may be even desired to set $p = 0$, and not considering the number of occurrences in some cases, see Section 7 for more details.

Resulting vector $\mathbf{b}'_f \in \mathbb{R}^K$ is dependent on the annotated experiment expt^+ , and the vectors computed based on different annotated experiments are not comparable with each other. Hence, we map values of $b'_{f,i}$ to $[0, 1]$ by using either softmax function or L_1 normalization as follows:

$$\hat{b}_{f,i} = \frac{\exp\{b'_{f,i}\}}{\sum_{j=1}^K \exp\{b'_{f,j}\}} \quad \text{or} \quad \frac{b'_{f,i}}{\sum_{j=1}^K b'_{f,j}}. \quad (5.5)$$

Resulting behavioral weight vector $\hat{\mathbf{b}}_f \in [0, 1]^K$ can be considered as a probability distribution. Here, the vector $\hat{\mathbf{b}}_f$ represents the behavioral characteristics of frame f of expt^- based on the behavioral repertoire of expt^+ . The voting-like scheme, which is used to finalize classification, incorporates all annotated experiments expt_r^+ considering corresponding $\hat{\mathbf{b}}_r$ behavioral weight vectors.

5.3.2

$$v_{f,i} = (\log_2(K) - H(\hat{\mathbf{b}}_f)) \hat{b}_{f,i} \quad \text{or} \quad \left(1 - \max_{1 \leq j \leq K} \hat{b}_{f,j}\right) \hat{b}_{f,i} \quad \text{or} \quad \hat{b}_{f,i} \quad (5.6)$$

$$\mathbf{v}_f = [v_{f,1}, \dots, v_{f,K}] \quad (5.7)$$

Chapter 6

Analyzing Behavioral Repertoire of Asleep Fruit Fly

Chapter 7

Employing Proposed Pipeline for Collected Data

Chapter 8

Results

Chapter 9

bast_y: A Software Package for Automated Behavioral Analysis of Asleep Fruit Fly

Chapter 10

Conclusion

Bibliography

- H. E. Rauch, C. T. Striebel, and F. Tung. Maximum likelihood estimates of linear dynamic systems. *AIAA Journal*, 3(8):1445–1450, August 1965. ISSN 0001-1452. doi: 10.2514/3.3166. URL <https://ui.adsabs.harvard.edu/abs/1965AIAAJ...3.1445R/abstract>.
- Gordon J. Berman, Daniel M. Choi, William Bialek, and Joshua W. Shaevitz. Mapping the stereotyped behaviour of freely moving fruit flies. *Journal of The Royal Society Interface*, 11(99):20140672, October 2014. doi: 10.1098/rsif.2014.0672. URL <https://royalsocietypublishing.org/doi/full/10.1098/rsif.2014.0672>. Publisher: Royal Society.
- Mayank Kabra, Alice A. Robie, Marta Rivera-Alba, Steven Branson, and Kristin Branson. JAABA: interactive machine learning for automatic annotation of animal behavior. *Nature Methods*, 10(1):64–67, January 2013. ISSN 1548-7105. doi: 10.1038/nmeth.2281. URL <https://www.nature.com/articles/nmeth.2281>. Number: 1 Publisher: Nature Publishing Group.
- Jesse D. Marshall, Diego E. Aldarondo, Timothy W. Dunn, William L. Wang, Gordon J. Berman, and Bence P. Ölveczky. Continuous Whole-Body 3D Kinematic Recordings across the Rodent Behavioral Repertoire - SI. *Neuron*, 109(3):420–437.e8, February 2021. ISSN 08966273. doi: 10.1016/j.neuron.2020.11.016. URL <https://linkinghub.elsevier.com/retrieve/pii/S0896627320308941>.
- Jeremy G. Todd, Jamey S. Kain, and Benjamin L. de Bivort. Systematic exploration of unsupervised methods for mapping behavior. *Physical Biology*, 14(1):015002, February 2017. ISSN 1478-3975. doi: 10.1088/1478-3975/14/1/015002. URL <https://doi.org/10.1088/1478-3975/14/1/015002>. Publisher: IOP Publishing.
- John G. Daugman. Uncertainty relation for resolution in space, spatial frequency, and orientation optimized by two-dimensional visual cortical filters. *JOSA A*, 2(7):1160–1169, July 1985. ISSN 1520-8532. doi: 10.1364/JOSAA.2.001160. URL <https://opg.optica.org/josaa/abstract.cfm?uri=josaa-2-7-1160>. Publisher: Optica Publishing Group.
- Christopher Torrence and Gilbert P. Compo. A Practical Guide to Wavelet Analysis. *Bulletin of the American Meteorological Society*, 79(1):61–78, January 1998. ISSN 0003-0007, 1520-0477. doi: 10.1175/1520-0477(1998)079<0061:APGTWA>2.0.CO;2. URL [http://journals.ametsoc.org/doi/10.1175/1520-0477\(1998\)079<0061:APGTWA>2.0.CO;2](http://journals.ametsoc.org/doi/10.1175/1520-0477(1998)079<0061:APGTWA>2.0.CO;2).
- Yonggang Liu, X. San Liang, and Robert H. Weisberg. Rectification of the

Bias in the Wavelet Power Spectrum. *Journal of Atmospheric and Oceanic Technology*, 24(12):2093–2102, December 2007. ISSN 1520-0426, 0739-0572. doi: 10.1175/2007JTECHO511.1. URL <http://journals.ametsoc.org/doi/10.1175/2007JTECHO511.1>.

Leland McInnes, John Healy, and James Melville. UMAP: Uniform Manifold Approximation and Projection for Dimension Reduction. *arXiv:1802.03426 [cs, stat]*, September 2020. URL <http://arxiv.org/abs/1802.03426>. arXiv: 1802.03426.

Leland McInnes, John Healy, and Steve Astels. hdbscan: Hierarchical density based clustering. *Journal of Open Source Software*, 2(11):205, March 2017. ISSN 2475-9066. doi: 10.21105/joss.00205. URL <https://joss.theoj.org/papers/10.21105/joss.00205>.

Ricardo J. G. B. Campello, Davoud Moulavi, and Joerg Sander. Density-Based Clustering Based on Hierarchical Density Estimates. In Jian Pei, Vincent S. Tseng, Longbing Cao, Hiroshi Motoda, and Guandong Xu, editors, *Advances in Knowledge Discovery and Data Mining*, Lecture Notes in Computer Science, pages 160–172, Berlin, Heidelberg, 2013. Springer. ISBN 978-3-642-37456-2. doi: 10.1007/978-3-642-37456-2_14.